A bioactive nanocomposite integrated specific TAMs target and synergistic TAMs repolarization for effective cancer immunotherapy

Wei Gu [a,1], Wen Guo [a,1], Zhishuang Ren [a], Yimeng Zhang [a], Meiqi Han [b], Qinfu Zhao [a], Yikun Gao [b], Yuling Mao [a,**], Siling Wang [a,*]

[a] *Department of Pharmaceutics, School of Pharmacy, Shenyang Pharmaceutical University, 103 Wenhua Road, Shenyang, Liaoning Province, 110016, China*
[b] *School of Life Sciences and Biopharmaceuticals, Shenyang Pharmaceutical University, 103 Wenhua Road, Shenyang, Liaoning Province, 110016, China*

ARTICLE INFO

ABSTRACT

Reactive oxygen species (ROS) generated from photosensitizers exhibit great potential for repolarizing immunosuppressive tumor-associated macrophages (TAMs) toward the anti-tumor M1 phenotype, representing a promising cancer immunotherapy strategy. Nevertheless, their effectiveness in eliminating solid tumors is generally limited by the instability and inadequate TAMs-specific targeting of photosensitizers. Here, a novel core-shell integrated nano platform is proposed to achieve a coordinated strategy of repolarizing TAMs for potentiating cancer immunotherapy. Colloidal mesoporous silica nanoparticles (CMSN) are fabricated to encapsulate photosensitizer-Indocyanine Green (ICG) to improve their stability. Then ginseng-derived exosome (GsE) was coated on the surface of ICG/CMSN for targeting TAMs, as well as repolarizing TAMs concurrently, named ICG/CMSN@GsE. As expected, with the synergism of ICG and GsE, ICG/CMSN@GsE exhibited better stability, mild generation of ROS, favorable specificity toward M2-like macrophages, enhancing drug retention in tumors and superior TAMs repolarization potency, then exerted a potent antitumor effect. *In vivo*, experiment results also confirm the synergistic suppression of tumor growth accompanied by the increased presence of anti-tumor M1-like macrophages and maximal tumor damage. Taken together, by integrating the superiorities of TAMs targeting specificity and synergistic TAMs repolarization effect into a single nanoplatform, ICG/CMSN@GsE can readily serve as a safe and high-performance nanoplatform for enhanced cancer immunotherapy.

1. Introduction

Tumor-associated macrophages (TAMs) represent a major constituent of the tumor microenvironment and are the most prevalent immune cells presented in solid tumors, accounting for up to 50% of the overall tumor cell population [1]. TAMs are predominantly derived from circulating peripheral blood monocytes. TAMs can be recruited to primary or metastatic tumors through various inflammatory signals released by cancer cells. Tumor cells "domesticate" the TAMs to become key paracrine partners, accelerating tumor progression and suppressing anti-tumor immune responses [2,3]. Therefore, immunotherapy against TAMs and the design of its delivery system is of great importance in the field of tumor therapy. Currently, the primary immunotherapeutic strategies targeting TAMs comprise hindering TAM recruitment, eliminating TAMs, and adjusting TAM polarization [4,5]. Macrophages are functionally flexible and, as is established, can polarize to the pro-inflammatory/anti-tumorigenic M1-like or anti-inflammatory/pro-tumorigenic M2-type [6,7]. However, TAMs are a diverse population and exhibit features more akin to the immunosuppressive M2-like phenotype that is pro-tumorigenic [8]. Fortunately, TAMs can be repolarized to the M1 phenotype in response to various environmental stimuli. This phenotype is capable of killing tumor cells by secreting proinflammatory cytokines, such as interleukin-1β (IL-1β), IL-12, and tumor necrosis factor-α (TNF-α) [9,10]. Furthermore, the repolarization of TAMs may mitigate tumor-associated immunosuppression and unleash an immune response against tumor cells, eventually leading to complete tumor eradication [11,12]. Repolarizing TAMs to the M1 phenotype for immune recovery is an attractive tumor

---

immunotherapeutic strategy [13,14]. Accordingly, TAMs are unsurprisingly linked to negative clinical outcomes in most cancers. Research into repolarization techniques for TAMs has produced several positive results, with reactive oxygen species (ROS)-mediated repolarization particularly promising. It has been shown that ROS can impact the polarization and activation of M1-like macrophages by regulating the signal transduction pathways of mitogen-activated protein kinase (MAPK) and NF-κB, which are linked to pro-inflammatory gene expression [15–17]. Furthermore, ROS generation can be stimulated through light irradiation, resulting in a targeted and localized effect with minimal adverse effects [18,19]. In immunotherapy, small molecule drugs, particularly ROS photosensitizers, have gained prominence [20]. Of these, indocyanine green (ICG), a clinically near-infrared light (NIR) fluorescent dye approved by the FDA for more than 60 years, can produce ROS when exposed to 808 nm NIR light irradiation with deeper tissue penetration depth and negligible irradiation damage [21,22].

Nowadays, ICG has been used extensively as clinically approved and is also considered as an important candidate to repolarize TAMs for antitumor immunotherapy [23,24]. While ICG is reasonably stable when associated with proteins in the bloodstream, its propensity to degrade as a concentrated aqueous stock solution means that ICG should be used shortly after reconstitution [25]. The application of ICG has been considerably impeded by several inherent limitations, which include inadequate light and hydrolytic stability, rapid clearance from the body, and significant off-target toxicity. Despite the excellent photothermal conversion capability of ICG, this photothermal instability hinders the practical application of ICG as a photothermal agent [26–28]. As a result, the use of ICG has become challenging in certain cases, ICG as drug delivery requires a specific carrier.

Efficient delivery systems should aim for both stability and precision targeting without subjective evaluation. Moreover, the M1-like-driven role of the drug delivery system presents a potential for combination therapy [29]. The development of nanotechnology offers new opportunities to overcome these limitations. It is beneficial to design an integrated nano-system that reduces systemic side effects and enhances the efficacy of repolarization for potent antitumor immunotherapy. Exosomes, ranging in size between 40 and 150 nm, are vesicles enclosed by a phospholipid membrane bilayer that are secreted by numerous cells [30]. They mediate intercellular communication by transferring molecular cargo - including nucleic acids, proteins, and lipids - to recipient cells, thereby regulating various functions in biological processes [31]. Alongside these intrinsic effects, exosomes are increasingly recognized as a promising option for drug delivery due to their excellent biocompatibility, long circulating half-life, appropriate size, and endogenous targeting ability [32]. Significantly, exosomes derived from plants can be produced on a large scale and display clear pharmacological actions on the human body, making them more appealing for therapeutic use than those derived from mammalian cells [33,34]. Based on these characteristics, exosomes derived from plants have been developed for the treatment of inflammatory diseases, cancer, and colitis [35]. Specifically, Cao et al. demonstrated that ginseng-derived exosomes, enriched with galactosyl monoacylglycerol, phosphatidyl ethanolamine, and ceramide, could be dominantly internalized by macrophages and suppress tumor growth by repolarizing TAMs, indicating their significant potential for antitumor immunotherapy [36]. To enhance the drug-carrying efficacy of exosomes, nanocarrier technology was used by comprising a nanocarrier kernel structure embedded within the exosome vesicle. Of the different nanocarriers, colloidal mesoporous silica nanoparticles (CMSN) have garnered considerable interest due to their biocompatibility, outstanding stability, ordered pore structure, and ease of modification, creating a nano environment that safeguards the encapsulated molecules from degradation and aggregation [37]. Accordingly, improved stability and dispersal of ICG with high cellular uptake efficiency may be achieved when it is encapsulated in nano-sized mesoporous silica cavities.

Inspired by this established evidence, we developed an integrated drug delivery system that includes the synergistic effects of repolarizing TAMs to enhance anti-tumor immunotherapy. We began by synthesizing CMSN as a basic nanoplatform to deliver ICG, resulting in ICG/CMSN. The mesoporous cavities in CMSN are anticipated to improve stability during biological transport and enhance ROS photogeneration, allowing for potential TAM repolarization. ICG/CMSN was coated with (GsE) to fabricate ICG/CMSN@GsE (Fig. 1). By adopting GsE, more nanoparticles can enter M2-like macrophages. Additionally, GsE can also inhibit tumor growth by modifying the repolarization of TAMs. Through integrating ICG and GsE into one nanoplatform, this designed drug-delivery system with synergistic repolarization of TAMs is expected to exhibit superior antitumor immunotherapeutic effects compared to monotherapy. This is the first use of ginseng exosomes in drug delivery to immune cells, and the composite system's design can serve as a theoretical reference for small molecule drug delivery and innovative ideas for combination therapy.

2. Results and discussion

2.1. Characterization of ICG/CMSN@GsE

CMSNs were firstly synthesized as basic nanocarriers to load ICG, and then the extracted GsE were coated on the surface of ICG/CMSN to finally obtain ICG/CMSN@GsE. Transmission electron microscopy (TEM) images (Fig. 2A) showed that the monodispersed CMSN, with well-ordered mesoporous structure, were spherical and the particle size was approximately 80 nm. GsE were presented as smooth bowl-shaped vesicles with integrity membranes. The mechanical force provided by ultrasonic energy could break the membrane structure of GsE and the incubation enables GsE to reassemble around CMSN to form a core-shell structure. As expected, the TEM image indeed showed the presence of a continuous membrane on the surface CMSN, confirming the successful attachment of GsE. In addition, the SDS-PAGE analysis exhibited that CMSN@GsE had similar protein bands in comparison with GsE (Fig. 2B), indicating that ultrasonic treatment had negligible influence on the exosome membrane proteins. The drug loading efficiency of ICG measured by working UV calibration curve (Fig. S1 and Table S1) was respectively 1.0%, 5.0%, and 26.5%, exhibiting that CMSN as a nanocarrier could achieve different drug loading efficiency by controlling the feeding ratio of ICG and GsE. N_2 adsorption/desorption isotherms and the corresponding BJH pore size distributions of the CMSN, ICG/CMSN of various drug loading efficiency, and CMSN@GsE nanoparticles are shown in Figs. S2 and 3. The specific BET surface area (S_{BET}), BJH pore diameter (W_{BJH}), and the cumulative pore volume (V_p) of related SNPs are listed in Tables S2–3. N_2 adsorption/desorption isotherms of CMSN display a typical IV isotherm. As expected, a slight decrease can be seen in terms of S_{BET} and V_p when the drug loading efficiency of ICG/CMSN nanoparticles was 1%, while the S_{BET} decreased from 821.2 m^2/g to 102.7 m^2/g and V_p decreased from 1.27 cm^3/g to 0.53 cm^3/g when the drug-loading efficiency was 26.5%. Significantly, when coated with GsE, the S_{BET} of CMSN sharply declined to 40.3 m^2/g, and no real pores were detected. The microstructure of ICG/CMSN coated with GsE was subsequently observed by atomic force microscopy (AFM). The scanning area was 2 μm $\times$ 2 μm, and the obtained 3D structural morphology is shown in Fig. 2C. A comparison of the microstructures of ICG/CMSN before and after GsE coating revealed that the ICG/CMSN@GsE spots were denser and more obvious. Meanwhile, the distribution of ICG/CMSN@GsE was more uniform, and different from the rough structural characteristics of ICG/CMSN surface before GsE coating, the surface of ICG/CMSN@GsE was smoother. Moreover, as shown in Fig. 2D and E, GsE coating did not alter the hydrodynamic particle size greatly, which increased from 144.5 $\pm$ 2.12 nm (CMSN) to 157.4 $\pm$ 2.18 nm (ICG/CMSN@GsE), while an obvious reversal of surface charge was observed with the ζ-potential decreased from +29.4 $\pm$ 1.18 mV (CMSN) to −10.6 $\pm$ 0.70 mV (CMSN@GsE), which was comparable to that of pure GsE (−11.3 $\pm$ 0.50 mV), further confirming the successful coating of GsE.
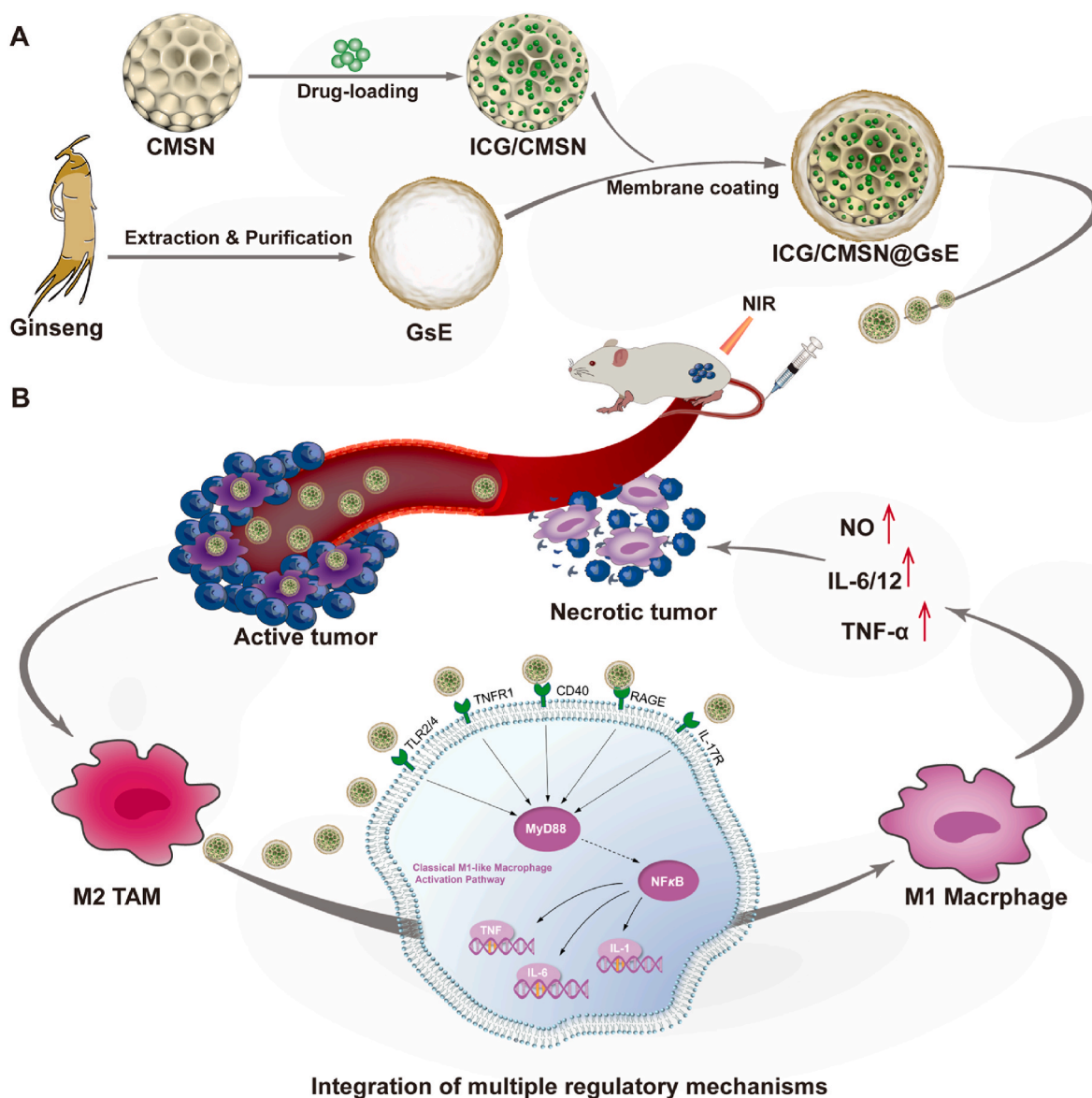
Fig. 1. Schematic illustration of preparation process and mechanism of ICG/CMSN@GsE for repolarizing TAMs.

Fig. 2F shows the color changes of free ICG, ICG/CMSN, and ICG/CMSN@GE samples at the same final concentration of ICG illustrating the masking effect of CMSN and GsE on ICG. At the same time, Fig. 2G shows the UV–vis–NIR absorbance spectrum of free ICG, CMSN, GsE, ICG/CMSN, and ICG/CMSN@GsE. The absorbance spectrum of ICG/CMSN and ICG/CMSN@GsE showed characteristic absorption peaks of ICG, while CMSN and GsE had no significant absorbance peak in that region. In addition, the absorbance peak intensity of ICG/CMSN@GsE was lower than that of ICG/CMSN, which also proved the successful loading of ICG and coating of GsE. These results indicated ICG was entrapped inside the CMSN and GsE coating could well block the exposed pores on the surface of CMSN. In conclusion, these results demonstrated the successful fabrication of ICG/CMSN@GsE.

2.2. Storage stability of ICG/CMSN@GsE and stability of ICG improved by CMSN@GsE

Following the successful establishment of ICG/CMSN@GsE, the stability of ICG/CMSN@GsE was evaluated in PBS and cell culture media with 10% serum, which is an extremely vital prerequisite for nanoparticles to be applied practically. Pleasingly, upon storage of 7 days in two different media, the ICG/CMSN@GsE remained well suspended without evident aggregation and no apparent change of particle sizes occurred during the monitoring period (Fig. 3A and B), demonstrating that ICG/CMSN@GsE could remain stable in blood circulation. Subsequently, the aqueous solution and light stability of ICG/CMSN@GsE were further investigated by monitoring the changes of UV–vis–NIR absorption spectra of ICG. For aqueous solution stability (Fig. 3D and E), the absorption peak intensity of free ICG was 0.69 within 48 h, and that of ICG in ICG/CMSN and ICG/CMSN@GsE remained 0.84 and 0.87, respectively. Significantly, the absorption peak intensity of ICG in ICG/CMSN and ICG/CMSN@GsE remained 0.39 and 0.53 even after 5 days, while free ICG sharply decreased to 0.04. Parallel studies were also carried out to determine the light stability of ICG/CMSN@GsE. The retention of ICG in ICG/CMSN and ICG/CMSN@GsE was 70.7% and 77.9% after 3 h under sunlight, dramatically higher than that of free ICG (38.2%). Such results demonstrated that CMSN and GsE could protect ICG from water and light damage. ICG/CMSN and ICG/CMSN@GsE (ICG NPs) exhibit good stability against photobleaching, while free ICG showed rapid photodegradation. The reason for the opposite photo-oxidative luminescence behavior of ICG NPs and free ICG is that ICG NPs showed a gradual enhancement of luminescence
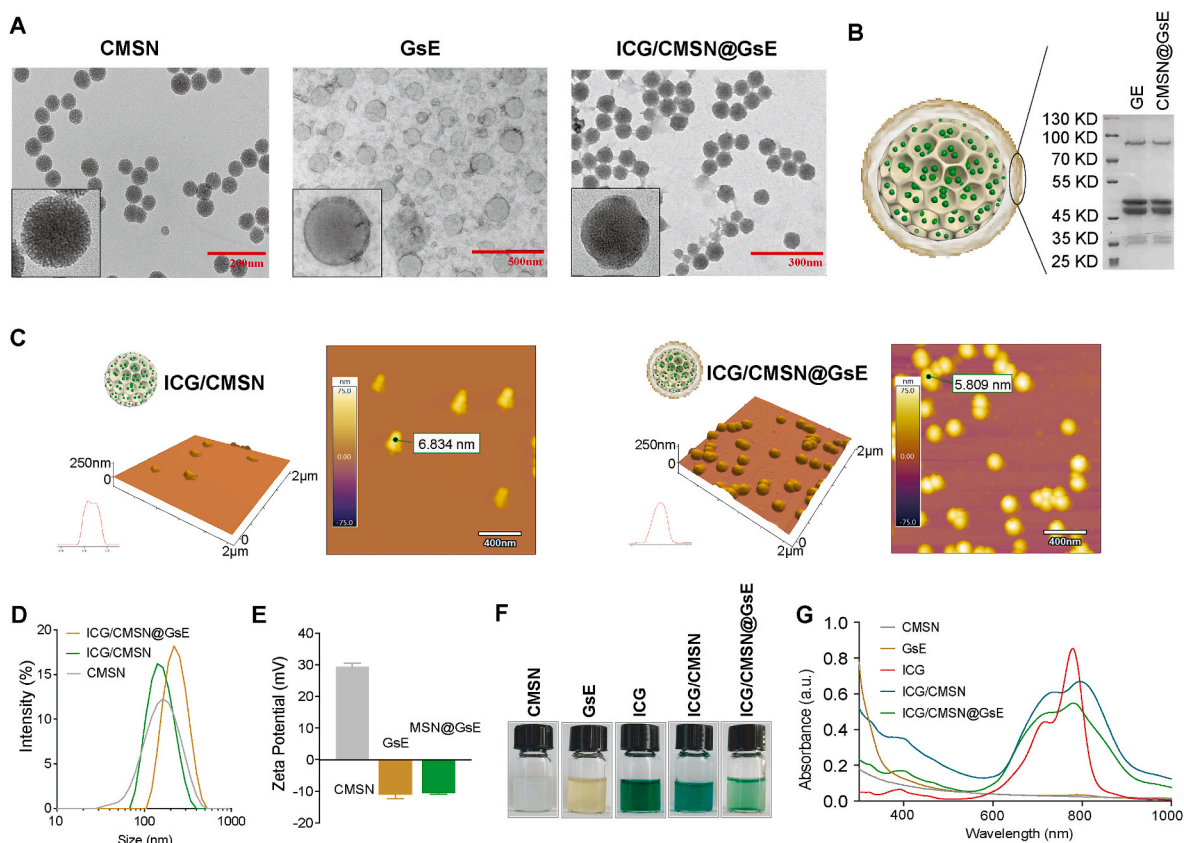
Fig. 2. Characterization of ICG/CMSN@GsE. (A) TEM characterization of CMSN, GsE, ICG/CMSN@GsE. (B) SDS-PAGE protein patterns of the marker, GsE, and CMSN@GsE. (C) The morphology and surface roughness of ICG/CMSN and ICG/CMSN@GsE were measured by AFM. (D) Hydrodynamic size of CMSN, ICG/CMSN AND ICG/CMSN@GsE. (E) ζ-potential of CMSN, GsE, and CMSN@GsE. (F) Photograph and (G) UV–Vis–NIR absorption spectra of CMSN, GsE, ICG, ICG/CMSN, and ICG/CMSN@GsE.

intensity under conditions of higher oxygen content. In comparison, free ICG showed gradual photo-oxidative degradation under conditions of higher oxygen content. The absorption spectra of the ICG NPs and the free ICG were analyzed, and it was found that the higher the oxygen content, the lower the absorbance of both ICG NPs and free ICG. For free ICG, this phenomenon is normal, i.e., the decrease in absorbance corresponds to the degradation of the chromophore; whereas for ICG NPs, the more pronounced the decrease in absorbance is, the higher the corresponding luminescence intensity is. This paradoxical phenomenon prompted the authors to hypothesize that an unstable intermediate product mediates this photo-oxidative luminescence enhancement of ICG NPs (Fig. 3C). A set of molecular dynamics simulations also supports this explanation: Amino acid derivative-mediated co-assembly of ICG forms an aggregate structure, in which the small molecular spacing between ICG molecules promotes the electron delocalization for two-photon absorption; during photoexcitation, singlet oxygen $^1O_2$ formed by energy transfer connects the carbon-carbon bonds between ICG molecules, and the resulting oxygenated dimer structure further expands to facilitate the electron delocalization for two-photon absorption, which ultimately enhances the fluorescence emission [38]. Consequently, all results indicated the potential stability of ICG/CMSN@GsE for improved cancer therapy.

2.3. ROS generation assessment

ROS, serving as second messengers in M1 signal transduction, is critical for the activation and function of M1-like macrophages. Given this, it would be necessary to better understand the ROS generation capability of ICG/CMSN and ICG/CMSN@GsE under exposure to NIR light. In this study, DPBF, which could irreversibly react with ROS,

resulting in a decrease of optical absorbance at 420 nm, was used as an indicator (Fig. 3G). As presented in Fig. 3F, free ICG exhibited a reduction in absorption of DPBF within only 4 min when irradiated with an 808 nm laser, implying the generation of abundant ROS. ICG/CMSN and ICG/CMSN@GsE, as reflected by absorbance change, exhibited a slower generation rate of ROS than free ICG. It's worth pointing out that mild generation of ROS is favorable for the repolarization of M2-like macrophages to M1 phenotype, in comparison with multiple ROS production within a short period, which would kill cells directly. As such, ICG/CMSN@GsE is expected to display the improved effects of the activation of M1-like macrophages.

2.4. Targeting ability of CMSN@GsE on M2-like macrophages and the mechanism of transcellular transport

The effective internalization of nanodrugs into macrophages is a prerequisite for the repolarization of M2-like macrophages. Therefore, a co-culture assay of M2-like macrophages and 4T1 cells was established to investigate the uptake specificity of CMSN@GsE. As shown in the flow cytometric analysis (Fig. 4A), the mean fluorescence intensity of CMSN@GsE in M2-like macrophages was 8.47-fold higher than that in 4T1 cells, suggesting CMSN@GsE could be internalized into M2-like macrophages more efficiently in comparison to 4T1 cells. Additionally, the mean fluorescence intensity in M2-like macrophages treated with CMSN@GsE was 2.12-fold higher than that treated with CMSN, indicating the efficient cellular uptake of CMSN@GsE by M2-like macrophages could be attributed to the coating of GsE. Moreover, the intracellular accumulation of CMSN@GsE in M2-like macrophages and 4T1 cells was further assessed by confocal laser scanning microscope (CLSM). After 2 h incubation with CMSN@GsE, M2-like macrophages
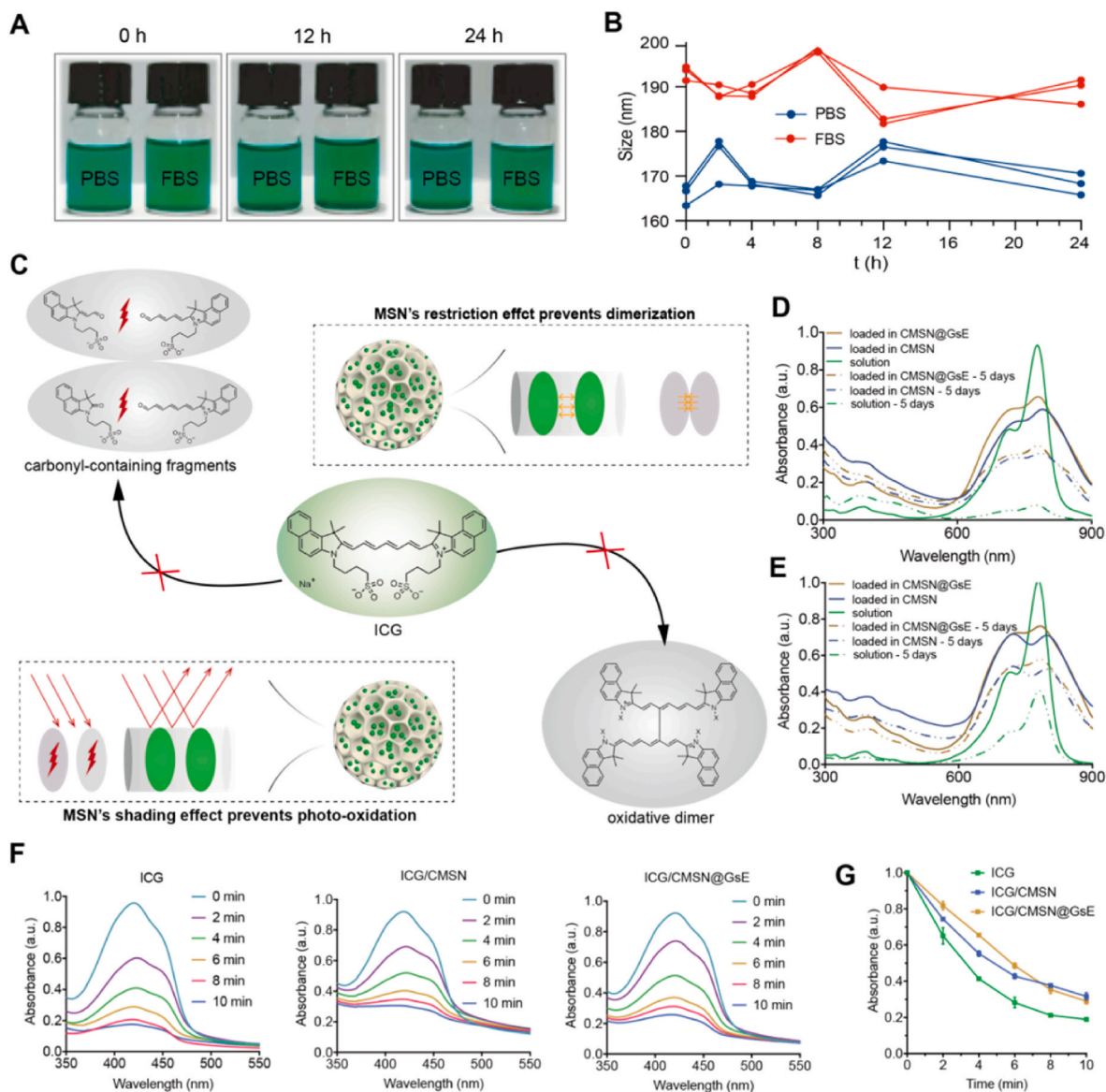
Fig. 3. Storage stability of ICG/CMSN@GsE and stability of ICG improved by CMSN@GsE. (A) Digital photographs of ICG/CMSN@GsE before and after being stored in different media for 24 h. (B) Changes in the particle size of ICG/CMSN@GsE in two different media for 24 h. (C) The influence of mesoporous skeleton on the stability of ICG. (D) UV–Vis–NIR absorption spectra changes of ICG, ICG/CMSN, and ICG/CMSN@GsE in aqueous solution for 5 days. (E) UV–Vis–NIR absorption spectra changes of ICG, ICG/CMSN, and ICG/CMSN@GsE under sunlight for 3 h. (F) ROS-induced absorbance changes of DPBF under 808 nm laser irradiation (0.75 W/cm^2) for different times. (G) Normalized absorbance changes at 420 nm of DPBF in different formulations.

showed a higher blue fluorescence signal than the 4T1 cells at the same conditions and CMSN@GsE co-localizes stronger than 4T1 with the nucleus and cell membrane in M2-like macrophages (Fig. 4B), demonstrating more efficient internalization of CMSN@GsE in M2-like macrophages, which coincided with the flow cytometry analysis results. In addition, the internalization process of CMSN@GsE in M2-like macrophages at 0.5 h, 1 h, and 2 h was also analyzed by CLSM and the results showed that the blue fluorescence signal and the red fluorescence signal were increased simultaneously with prolonged incubation (Fig. 4C). The above results demonstrated that the GsE coating endowed CMSN with superior capability of internalizing into M2-like macrophages.

To precisely discern the role of specific endocytosis pathways involved in the endocytosis of CMSN@GsE, 4T1 cells, and M2-like macrophages were pretreated with different endocytosis inhibitors. EIPA, Dynasore, Nystatin, Genistein, and CPZ-inhibited macropinocytosis, caveolae, and clathrin-mediated endocytosis were used to discriminate the endocytosis pathways involved. In the presence of

Dynasore, Nystatin, Genistein, and CPZ, the internalization of CMSN@GsE was significantly reduced in both cells, suggesting that caveolae and clathrin-mediated endocytosis played the same significant roles in the endocytosis of CMSN@GsE into 4T1 cells and M2-like macrophages (Fig. 4D). Interestingly, EIPA significantly inhibited the internalization of CMSN@GsE in M2-like macrophages but very little inhibition in 4T1 cells, suggesting that the macropinocytosis pathway was the minor route in the endocytosis of CMSN@GsE compared to clathrin- and caveolae-mediated endocytosis into 4T1 cell. Together, these results strongly indicated that clathrin-mediated and caveolae-mediated endocytosis dominated among endocytosis pathways of CMSN@GsE into 4T1 cells. Interestingly, the endocytosis pathways of CMSN@GsE into M2-like macrophages involved clathrin-mediated endocytosis, caveolae-mediated endocytosis, and even macropinocytosis. In summary, the internalization of CMSN@GsE into M2-like macrophages was via macropinocytosis for target intracellular delivery (Fig. 4E). The markedly different endocytosis pathways of CMSN/GsE by
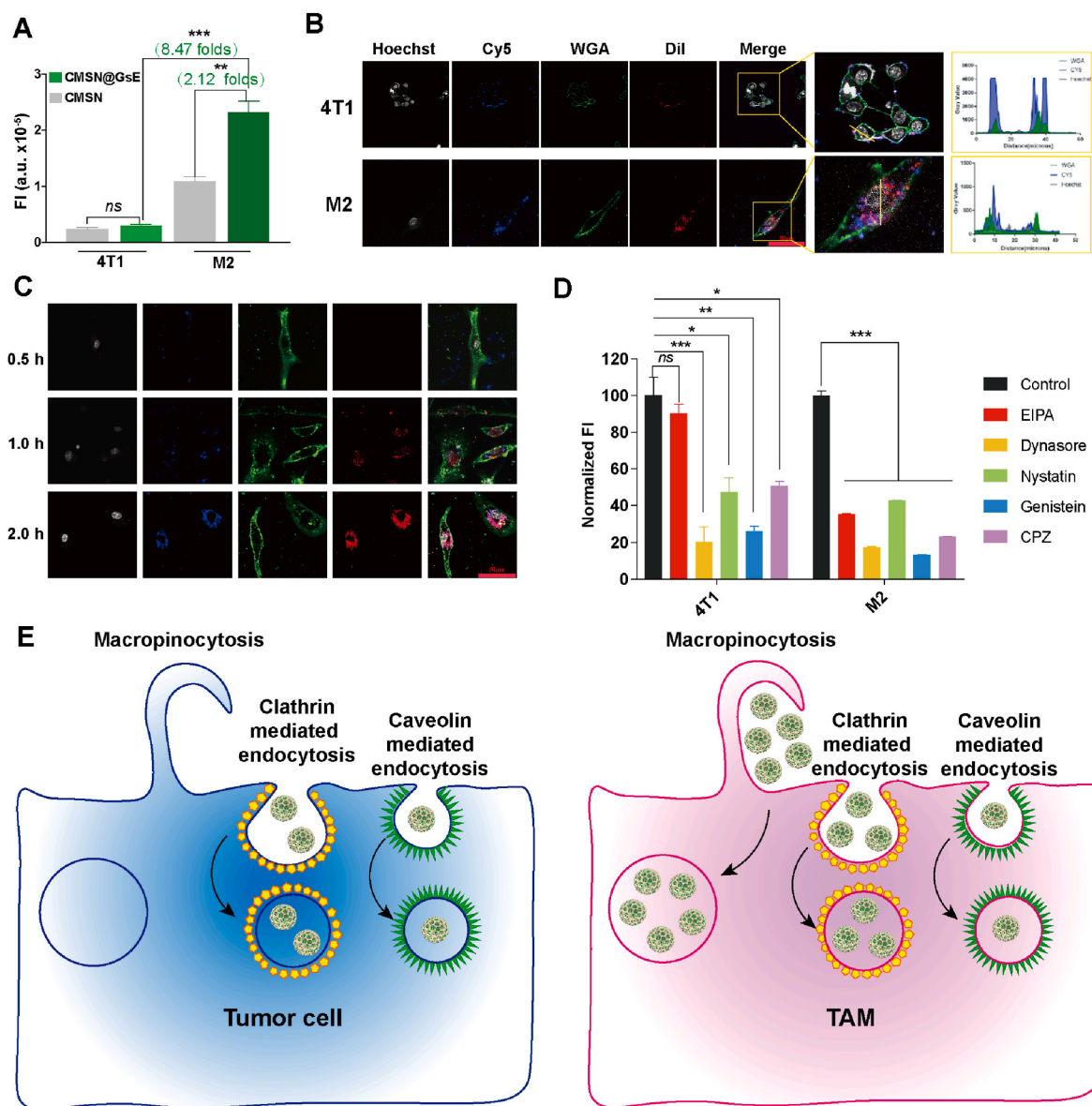
Fig. 4. **Significant targeted uptake of CMSN@GsE on M2-like macrophages.** (A) Mean fluorescence intensity of co-cultured M2-like macrophages and 4T1cells incubated with CMSN and CMSN@GsE, respectively. (B) CLSM images of M2 -like macrophages and 4T1 cells incubated with CMSN@GsE for 2 h. (C) CLSM images of M2-like macrophages incubated with CMSN@GsE at different times. (D) Impacts of various endocytosis inhibitors on the internalization of CMSN@GsE into 4T1 cells and M2-like macrophages. (E) Internalization of CMSN@GsE into M2-like macrophages via macropinocytosis for target intracellular delivery.

4T1 cells and M2-like macrophages result in a significant increase in the targeted uptake of CMSN@GsE by M2-like macrophages. This may be due to natural ligands on the exosome membrane, such as prostaglandin F2 receptor negative regulator (PTGFRN), that enhanced targeted drug delivery to TAMs [39]. As a very innovative concept, exploiting macropinocytosis for intracellular delivery of therapeutics into cells is emerging as a new drug delivery expedition with potential opportunities for cell-selective drug delivery [40].

2.5. Distribution and penetration of CMSN@GsE within tumors in vivo

To further verify the penetration effect of CMSN@GsE, the fluorescence intensity analysis was performed for tumors with different section depths. ICG/CMSN@GsE had the strongest fluorescence value in the tumor, which was significantly higher than that of ICG/CMSN and free ICG, overcoming the problem of poor drug penetration to improve tumor therapy efficiency (Fig. 5A and B). The dense extracellular matrix in tumors usually limits the nanomedicines to penetrate deep tumors,

leading to insufficient therapeutic efficiency [41]. These results indicated that the incorporation of GsE endowed ICG/MSN specific permeability for tumor accumulation. Based on the demonstrated superior specificity of ICG/CMSN@GsE toward M2-like macrophages in vitro, the tumor accumulation performance of ICG/CMSN@GsE was further evaluated in 4T1 tumor-bearing mice by monitoring the fluorescence signal of ICG using an Interactive Video Information System optical imaging system at different time points post intravenous injection of various nano-formulation. As illustrated in Fig. 5C and D, both ICG/CMSN-treated and ICG/CMSN@GsE-treated mice exhibited the strongest fluorescence intensity in tumor regions at 3 h post-injection and then reduced gradually. Noticeably, the mean fluorescence intensities in tumor sites at 3 h and 24 h of ICG/CMSN@GsE-treated mice were 1.6-fold and 1.5-fold higher than that of ICG/CMSN-treated mice, respectively. In addition, ICG/CMSN@GsE also showed higher semi-quantitative fluorescence intensity in major organs and tumors compared to the ICG/CMSN group at 24 h postinjection (Fig. 5E), demonstrating that ICG/CMSN@GsE displayed superior tumor
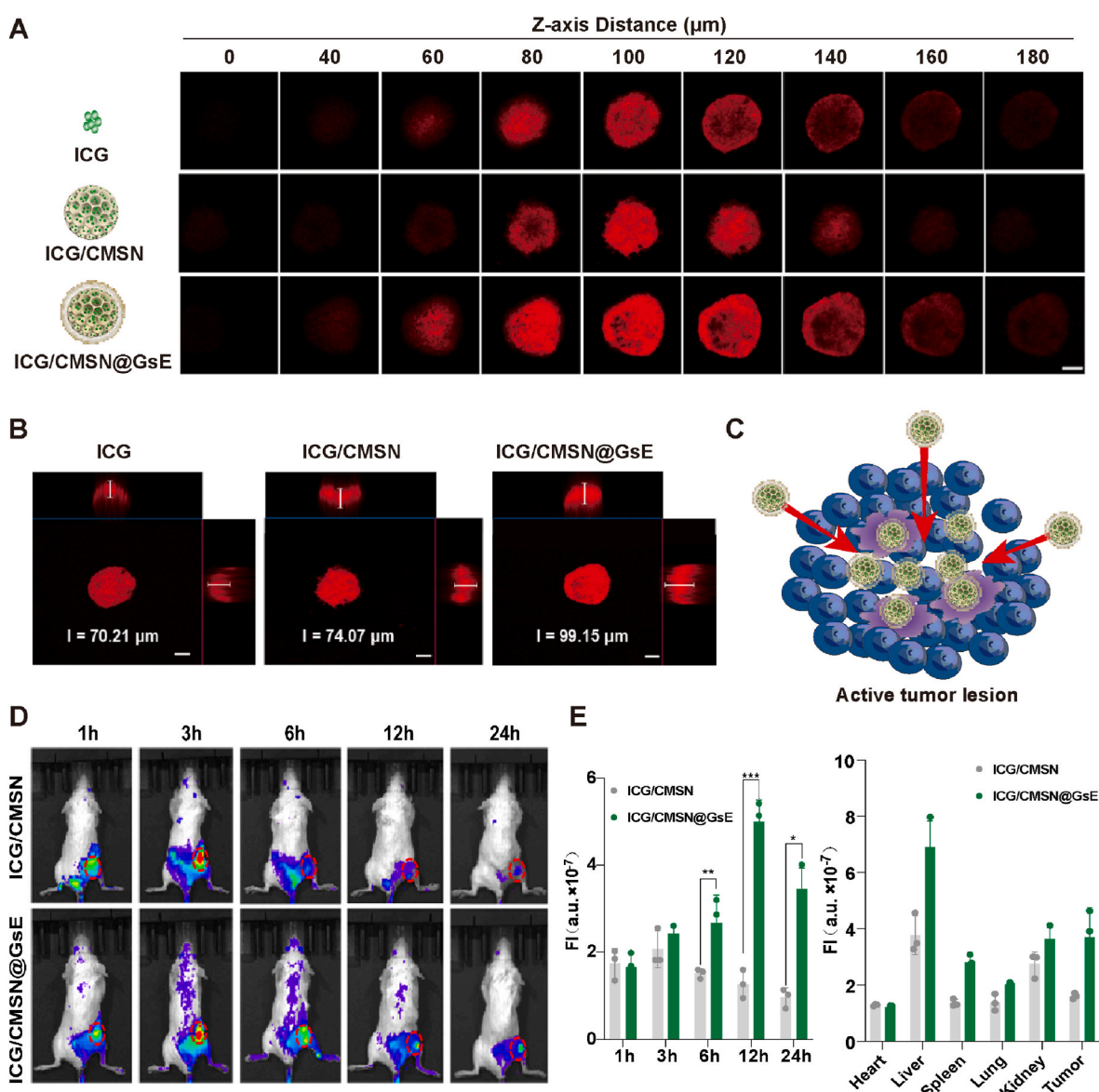
Fig. 5. ICG/CMSN@GsE improves retention time in the circulation and specific tumor accumulation. (A) Fluorescence images of tumor cross-sections at different depths after treatment with ICG, ICG/CMSN, ICG/CMSN@GsE for 24 h and (B) Depth of penetration corresponding to the strongest fluorescence value. (C) ICG/CMSN@GsEs penetrate deep tumor lesions. (D) *In vivo* fluorescence images of tumor-bearing mice after treatment with ICG/CMSN, ICG/CMSN@GsE at the designated time points (n = 3). (E) Semi-quantitative fluorescent intensity of tumors overtime during *in vivo* imaging and semi-quantitative fluorescent intensity of tumors and major organs at 24 h post-injection.

accumulation ability. Considering the fluorescence of ICG/CMSN@GE was generally higher than ICG/CMSN, a percentage of fluorescence signal post 24 h injection was displayed for the comparison to normalize the data (Fig. S4). The results also proved that the higher fluorescence of ICG/CMSN@GsE was caused by the incorporation of GsE, endowing ICG with longer circulation in the blood and tumor-specific accumulation.

2.6. Cell viability analysis

The ROS generated by ICG under NIR irradiation can repolarize M2-like macrophages to the M1 phenotype, but abundant ROS would cause cell necrosis. Thus, it's extremely vital to optimize the concentration of ICG to ensure that macrophages have high cell viability (over 90%), which is a prerequisite for the repolarization of M2-like macrophages. It is noteworthy that, in this study, CMSN was employed to load ICG, and GsE was coated on the surface of CMSN to improve the stability of ICG and exert synergistic TAMs repolarization effect. Therefore, lowering

the drug loading efficiency of ICG/CMSN rationally would be a breakthrough in achieving the above-mentioned goal. As indicated by the CCK-8 assay (Fig. S5), the viabilities of M2-like macrophages displayed dependences on the concentration of ICG. In addition, when the drug loading efficiency of ICG/CMSN@GsE was 1%, the viability of macrophages decreased by less than 90% at the ICG concentration of 4 µg/mL, which might be related to the damage by the excessive nanoparticles. It is very impressive that, for the 5% drug loading efficiency group, the M2-like macrophages, after incubation with ICG/CMSN@GsE at ICG concentrations up to 15 µg/mL, exhibited superior viability above 90%. Therefore, the optimal drug loading efficiency of ICG/CMSN@GsE was determined to be 5% and a 15 µg/mL administration amount of ICG was chosen for further experiments. In addition, considering that ICG/CMSN@GsE may be taken up by non-specific macrophages such as M1-like macrophages, the potential toxicity of the formulation to M1-like macrophages was examined in Fig. S6. The results showed that cell survival remained above 70% at 20 µg/mL concentration of ICG.

2.7. Repolarization of M2-like macrophages and anti-tumor activity of ICG/CMSN@GsE in vitro

After performing *ex vivo* and *in vivo* targeting validation of ICG/CMSN@GsE, we verified the ability of ICG/CMSN@GsE to repolarize M2-like macrophages and produce M1-like macrophage-associated cytokines (Fig. 6A), which resulted in enhanced anti-tumor activity (Fig. 6E). Having investigated the optimal administration amount of ICG/CMSN@GsE, their repolarization effect on M2-like macrophages was evaluated by flow cytometry anlysis. As shown in Fig. 6B and C, the ICG/CMSN group exhibited a negligible increase in the expression level of M1-related typical biomarker CD86 (7.64 ± 0.51%), which increased by 3.0-fold in the ICG group (2.38 ± 0.24%), owing to the improved stability of ICG mediated by CMSN. In addition, compared to the ICG/CMSN + GsE group, the expression level of CD86 in the ICG/CMSN@GsE group significantly increased to 28.15 ± 0.64%, while M2-related typical biomarker CD206 decreased to 5.20 ± 1.82%, suggesting a more satisfactory phenotypic transformation from M2 to M1. Furthermore, ELISA assays showed (Fig. 6D), compared with the control groups, the M1 macrophage-related cytokines (TNF-α, NO, and IL-12) were markedly upregulated by ICG/CMSN@GsE under an 808 nm laser irradiation, which was consistent with the quantitative results of flow cytometry (FCM). Evaluating the anti-tumor activity of ICG/MSN@GsE through apoptosis assay (Fig. 6F). With a cell survival rate of 93.4% in the untreated group, indicating good cell status. The ICG/CMSN, GsE and ICG/CMSN@GsE under laser groups all showed varying degrees of cell apoptosis and necrosis, while the anti-tumor activity of ICG/CMSN@GsE was the highest, totaling 32.4%. The above results collectively indicated that ICG/CMSN@GsE could repolarize M2-like macrophages to the M1 phenotype more efficiently.

2.8. Analysis of messenger RNA transcripts (immune cell-associated genes) for M2-like macrophage differentiation 24 h after administration of ICG/CMSN or ICG/CMSN@GsE

Emerging evidence supports the theory that ginseng exosomes can regulate important regulatory factors associated with macrophage phenotype [42]. To determine the mechanism by which ICG/CMSN@GsE mediates the repolarization of M2-like macrophages, we used high-throughput sequencing (RNA-seq) to analyze mRNA in M2-like macrophages, and M2-like macrophages untreated with ICG/CMSN or ICG/CMSN@GsE served as control samples. First, induction of M2-like macrophages was achieved by IL-4, and macrophages undergoing functional reprogramming were obtained and subjected to RNA-seq after 48 h by washing and co-incubation with ICG/CMSN or ICG/CMSN@GsE (Fig. 7A). In ICG/CMSN or ICG/CMSN@GsE-treated M2-like macrophages, 248 and 375 up-regulated mRNAs were identified, respectively, with 93 mRNAs overlapping, and more differentially expressed mRNAs and a larger percentage of up-regulated mRNAs were found in the sequencing results of ICG/CMSN@GsE-treated M2-like macrophages (Fig. 7B and C). To explore the mechanistic differences between ICG/CMSN and ICG/CMSN@GsE on the mRNA expression levels in M2-like macrophages, the most prominent biochemical metabolic pathways and signaling pathways involved in the differentially expressed genes (log FC > 1 and P-Value <0.05) were clustered and analyzed by Pathway significance enrichment to generate a differentiated between the two sets of Kyoto Encyclopedia of Genes and Genomes (KEGG) metabolic pathway bubble diagrams (Fig. 7D and E). Compared
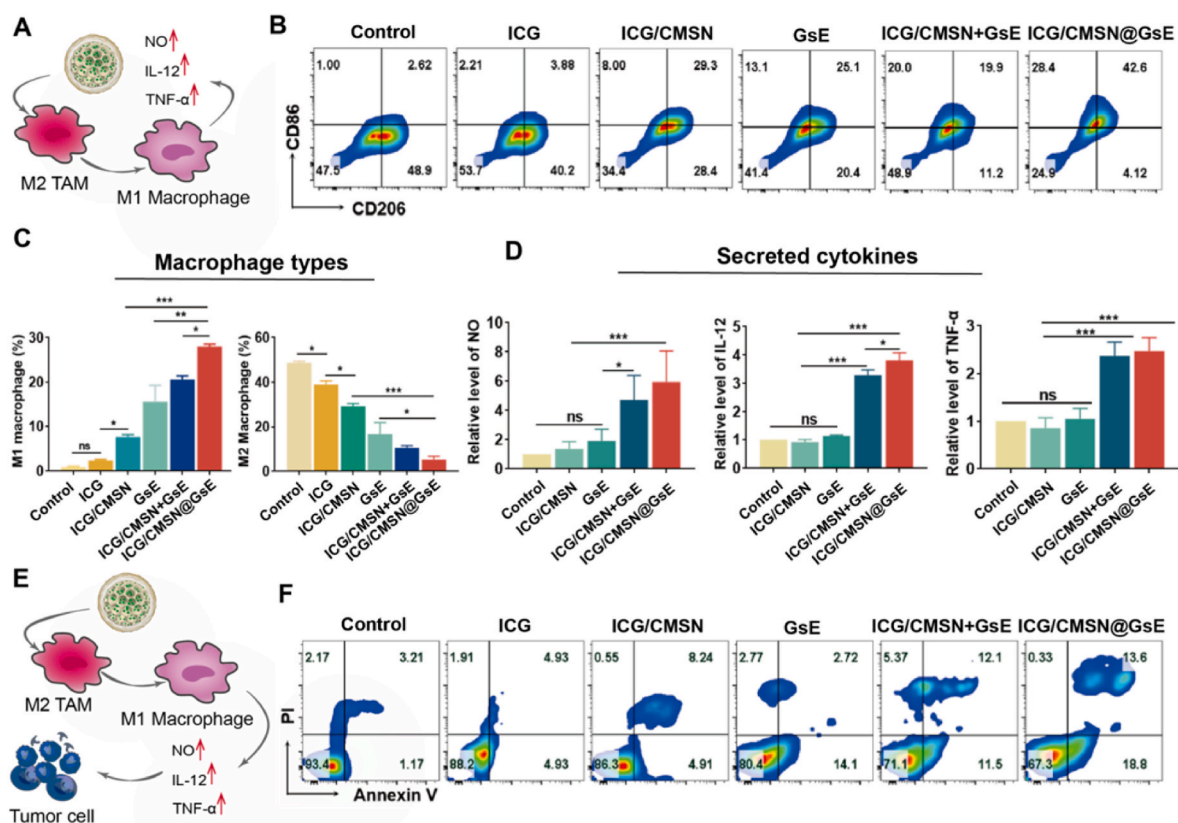

Fig. 6. Repolarizing and antitumor activity of ICG/CMSN@GsE on M2-like macrophages. (A) Schematic diagram of ICG/CMSN@GsE repolarizing M2-like macrophages to produce M1-like macrophage-associated cytokines. (B) Flow cytometric analysis of expression of CD86 and CD206 after co-culturing M2-like macrophages with different formulations. Relative quantification of (C) M2-like macrophages (CD206+) and M1-like macrophages (CD86+). (D) The levels of NO, TNF-α, and IL-12 were assayed by ELISA after treating M2-like macrophages with different formulations. (E) Schematic diagram of ICG/CMSN@GsE repolarizing M2-like macrophages thereby enhancing antitumor activity. (F) Representative images of flow cytometric analysis of cell apoptosis in different treated 4T1 cells.
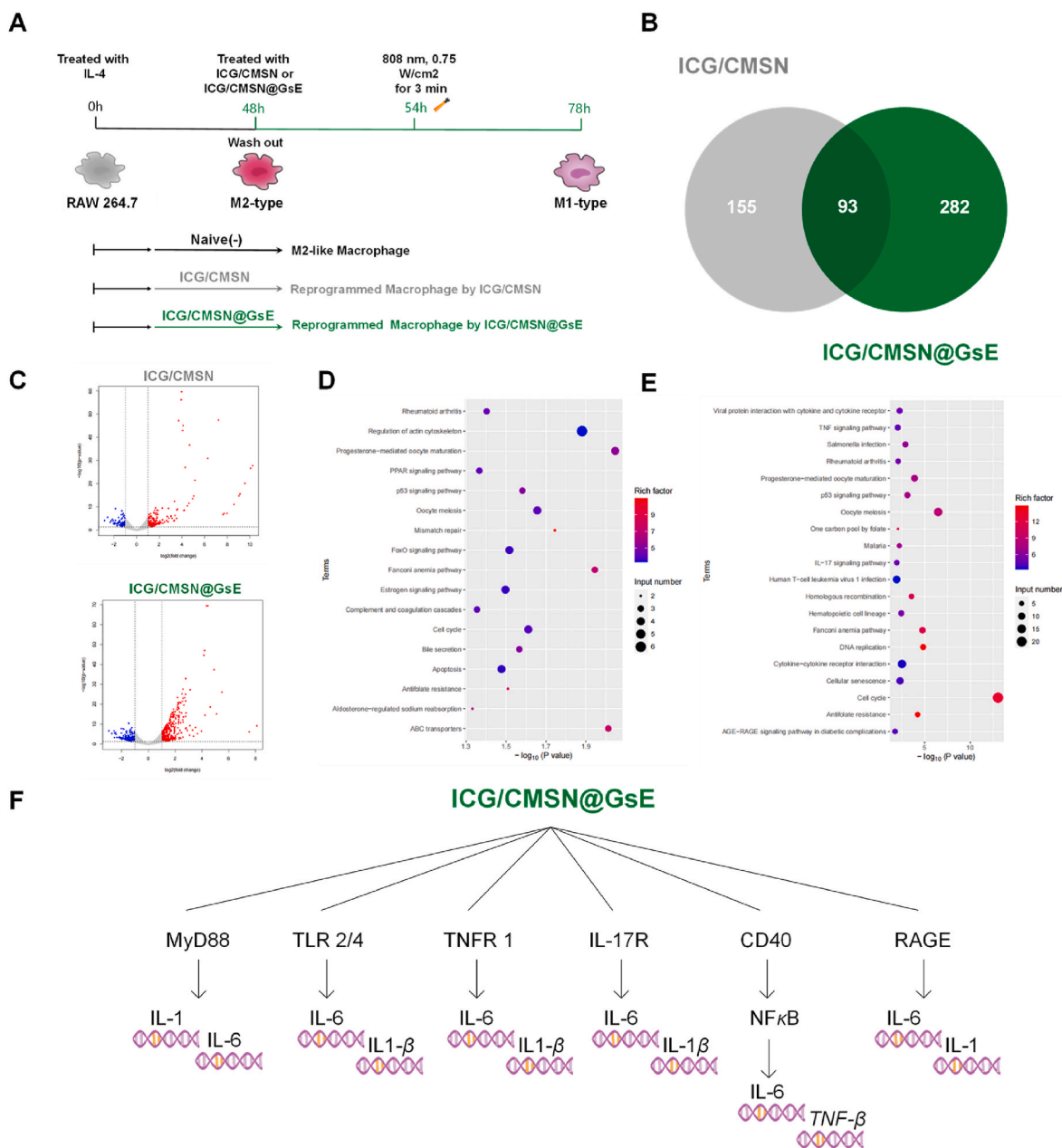
Fig. 7. mRNA expression of ICG/CMSN@GsE. (A) Schematic representation of induction of M2-like macrophages and reversal by treatment of ICG/CMSN or ICG/CMSN@GsE. (B) Venn diagram of complete and overlapping mRNAs presented by ICG/CMSN or ICG/CMSN@GsE. (C) Volcano map of mRNAs expression. (D) KEGG metabolic pathway map of up-regulated genes by ICG/CMSN or (E) ICG/CMSN@GsE. (F) Speculative map of the signaling pathway activated by ICG/CMSN@GsE.

with the ICG/CMSN-treated group, the ICG/CMSN@GsE-treated group was enriched for 15 classical or non-classical M1-like macrophage activation pathways and was particularly enriched for the TNF signaling pathway, human T-cell leukemia virus 1 infection, and rheumatoid arthritis, etc. The main mRNAs enriched in these pathways were IL-1, IL-1β, and IL-6, which are all involved in the regulation of M1-like macrophages. Then, we explored the mechanism by which ICG/CMSN@GsE stimulates the transformation of M2-like macrophages to M1-like, and analyzed the key genes according to the major immune-related signaling pathways. As shown in Fig. 7F, ICG/CMSN@GsE can enter into the nucleus mediated by a variety of membrane receptors, such as TNFR1, CD40, and RAGE, and increase its transcriptional level, followed by significant upregulation of upstream genes like MyD88 and NFκB, which finally promote the expression of signaling molecules IL-1, IL-6 and so on, which is consistent with previous reports [43–45]. In conclusion, the ICG/CMSN@GsE composite

delivery system was able to reverse the macrophage phenotype and effectively promote the transformation of M2-like macrophages to M1-like macrophages.

2.9. Evaluation of immunotherapeutic effect

The above positive results encouraged us to evaluate the immunotherapeutic efficacy of ICG/CMSN@GsE *in vivo*. To this end, 4T1 tumor-bearing mice were randomly divided into six groups and individually treated with normal saline, ICG, ICG/CMSN, GsE, ICG/CMSN + GsE and ICG/CMSN@GsE every two days for four times (Fig. 8A). It was found that there was no obvious variation in body weights among each group (Fig. S7), preliminarily suggesting that all formulations displayed no obvious systemic toxicity. In addition, as shown in Fig. 8B–D, in comparison to the sustained tumor growth of mice treated with ICG, a noticeable size reduction of tumors was found in the ICG/CMSN group
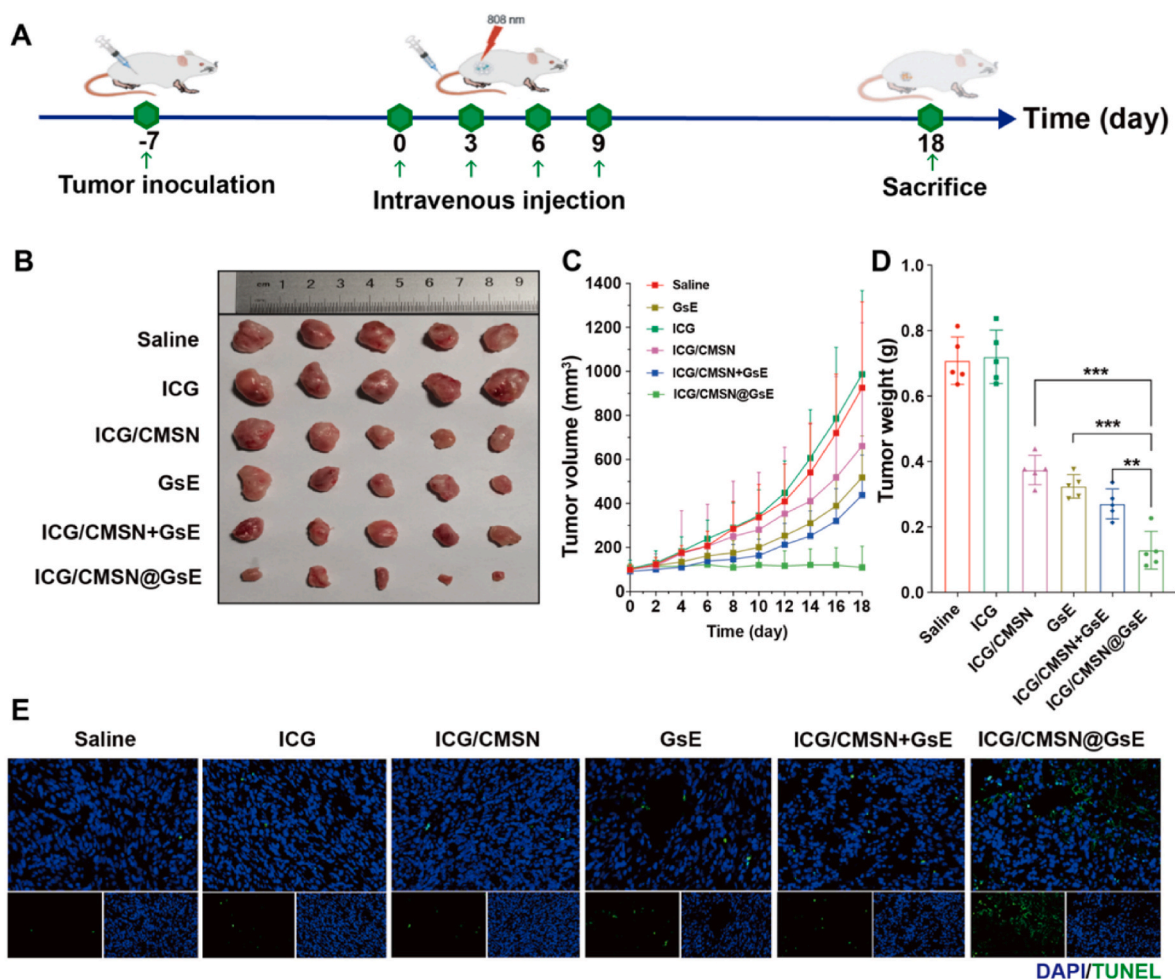
Fig. 8. Evaluation of the anti-tumor ability of ICG/CMSN@GsE. (A) Schedule of *in vivo* administration approach. (B) Images of tumor tissues isolated from mice in different therapy groups. (C) The relative tumor volume growth curves of tumor-bearing mice during treatments. (D) Tumor weights of the sacrificed mice on day 18 of treatment. (E) Representative tunnel staining images of tumor tissues were obtained at the study endpoint.

with a tumor inhibition rate of 47.3%. In particular, compared with all other groups, tumor development was considerably delayed by ICG/CMSN@GsE, and the tumor inhibition rate reached 81.9% with the cooperation of ICG/CMSN and GsE. Furthermore, the end-point tumor weights of different treatment groups further affirmed the best inhibitory effect of ICG/CMSN@GsE on tumor growth (Fig. 8D). Finally, as the representative TUNEL staining results revealed (Fig. 8E), the tumor tissues obtained from the ICG/CMSN@GsE treated mice displayed maximum necrosis and apoptosis among all groups, in line with the above results.

Subsequently, immunofluorescent and histochemical staining were performed to further verify the immunotherapeutic effect and safety of ICG/CMSN@GsE. The repolarization of TAMs in tumor tissues of mice receiving various treatments was assessed by determining M1-related biomarker CD86 and M1-related biomarker CD206 with IF staining. As shown in Fig. 9A, the tumor tissues of mice treated with ICG exhibited strong green fluorescence of CD206, which matched the fast tumor growth. In comparison, mice treated with ICG/CMSN, GsE, and ICG/CMSN + GsE showed reduced green fluorescence of CD206 and increased pink fluorescence of CD86 in the tumor tissues, confirming the repolarization of M2-like TAMs to M1 phenotype. As expected, ICG/CMSN@GsE treated mice showed the best TAM repolarization effect with the lowest green fluorescence intensity of CD206 and the highest pink fluorescence intensity of CD86 in the tumor tissue, which would effectively facilitate the apoptosis of tumor cells.

Immunohistochemical (IHC) results showed that the expression

levels of inflammatory markers IL-6, iNOS, and TNF-α were significantly elevated in each of the ICG, ICG/CMSN, GsE, ICG/CMSN + GsE, and ICG/CMSN@GsE treatment groups, compared to the control group, which received saline treatment alone (Fig. 9B). This observation highlights the potential role of these treatment strategies in promoting inflammatory responses. Notably, the ICG and GsE groups alone were particularly prominent in the expression of IL-6 and TNF-α, possibly reflecting the superior phototherapy effect of ICG under NIR light irradiation, as well as the intrinsic therapeutic potential of GsE in addition to the delivery of drugs. In particular, the ICG/CMSN@GsE group was the most remarkable in terms of iNOS expression, which may reveal the unique mechanism of ICG/CMSN@GsE in regulating the reversal of TAM repolarization. Considering the safety of the formulation, targeting efficiency, and ability to reverse TAM polarization, ICG/CMSN@GsE demonstrates the potential to maximize the effects of cancer immunotherapy while ensuring *in vivo* safety. In addition, H&E staining of main organs was carried out and the results indicated no obvious lesions were found in any group (Fig. S8), further indicating their systemic biosafety. In sum, these results consistently confirmed that due to the favorable synergism of ICG/CMSN and GsE, the anticancer effect of ICG/CMSN@GsE can be effectively enhanced by repolarizing TAMs to M1 phenotype with no noticeable systemic toxicity.

3. Conclusion

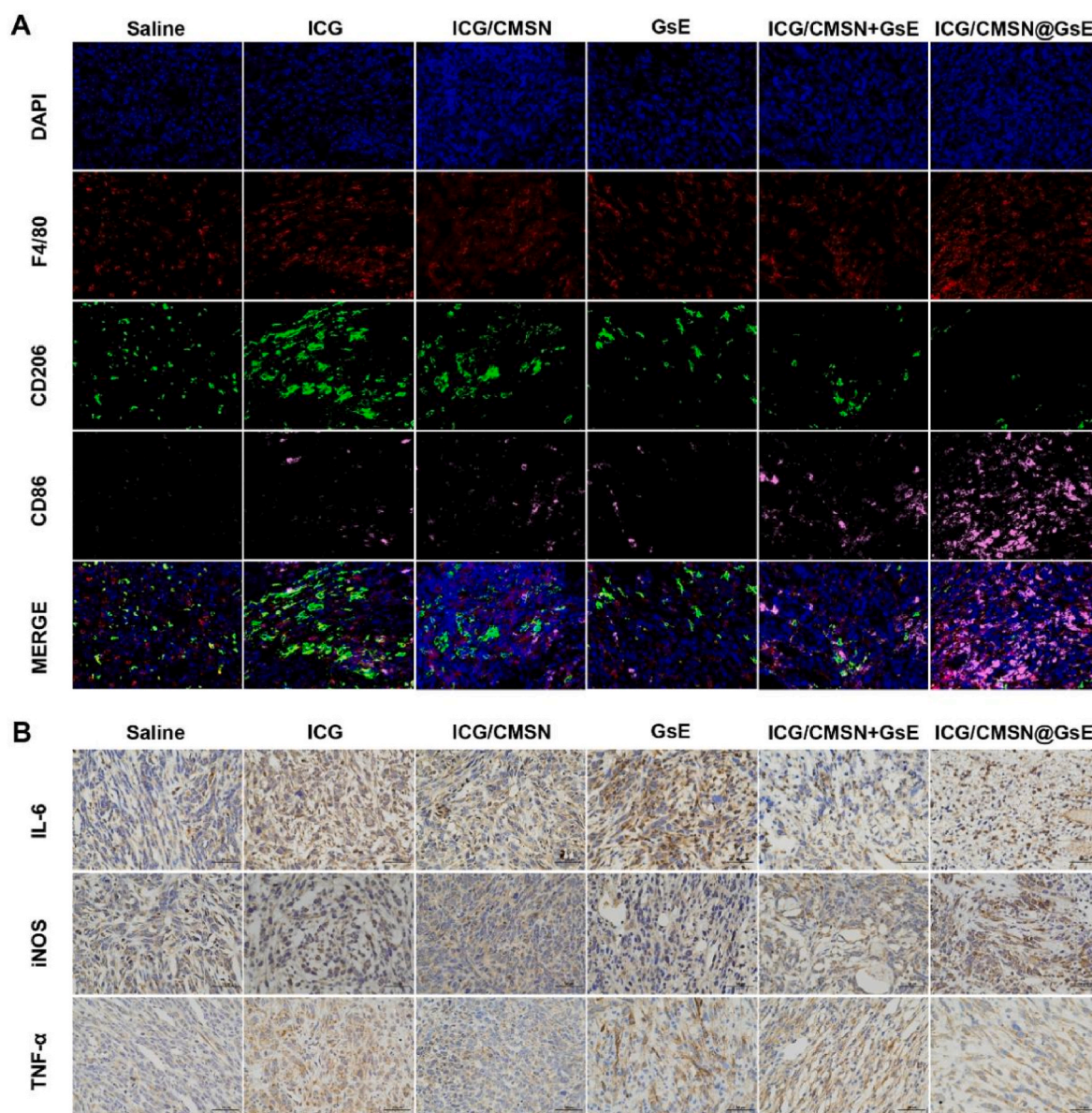In the study, an integrated nano platform (ICG/CMSN@GsE) was

Fig. 9. Evaluation of the immunotherapeutic effect of ICG/CMSN@GsE. (A) Representative immunofluorescence images for F4/80 (red), CD206 (green) and CD86 (pink). (B) Analysis of tumor apoptosis after treatment as shown by IHC staining.

successfully developed by encapsulating the ICG-loaded CMSN with GsE. ICG/CMSN@GsE exhibited enhanced stability and gentle ROS photogeneration, which was advantageous for the activation of M1 macrophages. Besides, the improved antitumor immunotherapy is achieved through the targeted and synergistic repolarization capacity of ICG/CMSN@GsE, which results in a favorable polarization effect. This leads to the upregulation of pro-inflammatory cytokines like TNF-α and IL-12. As a result, a strong anticancer effect is obtained. Overall, this work demonstrates a straightforward approach for creating a secure and high-performance nano platform, which coordinates the repolarization of M2-like TAMs to M1 phenotype, and consequently enhances the effectiveness of antitumor immunotherapy.

4. Materials and methods

4.1. Materials

Hexadecyl trimethyl ammonium chloride (CTAC, >99%) was obtained from Sinopharm Group Chemical Reagent Co., LTD (Shenyang,

China). Triethanolamine (TEA, >95%) was purchased from Tianjin Bodi Chemical Co., Ltd (Tianjin, China). Tetraethoxysilane (TEOS, 98%) was purchased from Sigma-Aldrich (Shanghai, China). ICG, 1,3-diphenyl isobenzofuran (DPBF), membrane protein extraction kit, Annexin V-FITC apoptosis detection kit, 3-(4,5-dimethylthiazol-2-yl)-2,5- diphenyltetrazolium bromide (MTT), cholecystokinin octapeptide (CCK-8) assay kit, Dulbecco's Modified Eagle's Medium (DMEM), RPMI 1640, PBS (pH 7.4), fetal bovine serum (FBS), 100 U/ml penicillin and 100 mg/ml streptomycin were all purchased from Meilun Biotechnology Co., Ltd (Dalian, China). Nitric oxide (NO) assay was acquired from Solarbio Science & Technology Co., Ltd. (Beijing, China). The mouse interleukin 12 (IL-12), mouse tumor necrosis factor-alpha (TNF-α) uncoated enzyme-linked immunosorbent assay (ELISA) kits, FITC-labeled F4/80, PE-labeled CD206 and APC-labeled CD86 monoclonal antibody were purchased from Thermo Fisher Scientific.

4.2. Synthesis of CMSN

CMSNs were synthesized by the method reported in our previous

work [46]. In preparation of Amino-functionalized CMSN, 0.8 mL APTES was added into 100 mL ethanol suspension of redispersed CMSN with stirring and circulation reflux at 80 °C for 12 h. Template extraction was carried out in hydrochloric acid-ethanol solution (15 ml 37% HCl in 120 ml ethanol) under heating to 70 °C for 24 h. The products were collected and washed with ethanol and deionized water three times respectively by repeated centrifugation (11,000 rpm, 6 min).

4.3. Loading ICG into CMSN (ICG/CMSN)

ICG/CMSN was prepared by adding 0.2, 1, 6 mL ICG (1 mg/mL) into 5 mg/mL CMSN aqueous suspension (3.96, 3.8, 2.8 mL) respectively with the final solution volume of 10 mL. The mixture was stirred for 24 h at room temperature and protected from light. The unloaded ICG molecules were washed with deionized water and centrifuged at 11,000 rpm. The supernatant was collected and measured via a UV–vis spectrometer at 780 nm to determine the drug-loading capacity (LC) according to the following formula:

$$Loading\ capacity\ (\%) = \frac{Weight_{ICG}}{Weight_{ICG/CMSN}} \times 100$$

4.4. Isolation of ginseng exosomes (GsE)

Ultracentrifugation was used to extract the GsE according to previous studies. The ginseng root juice was centrifuged at increasing speeds ($1000 \times g$ for 10 min, $3000 \times g$ for 20 min, and $10,000 \times g$ for 30 min) to remove large particles and fibers. Then the supernatant was ultracentrifuged at $100,000 \times g$ for 1 h, and the pellets were resuspended in PBS, subjected to a gradient sucrose solution (15, 30, 45, and 60%), and ultracentrifuged at $150,000 \times g$ for another 1 h. The band between the 30% and 45% sucrose layer was collected and diluted in PBS followed by ultracentrifuging at $150,000 \times g$ for 1 h. Finally, the pellets were resuspended in PBS and stored at −80 °C until further use.

4.5. Preparation of GsE-coated nanoparticles (ICG/CMSN@GsE)

GsE were coated on the surface of ICG/CMSN via sonication of 5 cycles. Concisely, the process of sonication (500 V, 2 kHz, 20% power, 15 s on/30 s off) for 3 times followed by 2 min time intervals was defined as 1 cycle. GsE at a protein concentration of 2.3 mg/mL (particle concentration of $(2.48 \pm 0.57) \times 10^9$ particles/mL) and 2 mL of ICG/CMSN (100 μg/mL) were mixed and treated with the sonication described above in an ice bath. The mixture was further brewed at 37 °C for 1 h to recover the membrane of GsE. The final product was collected and washed with PBS three times and lyophilized to obtain ICG/CMSN@GsE for further use.

4.6. Characterization of ICG/CMSN and ICG/CMSN@GsE

The morphologies of CMSN, GsE, and ICG/CMSN@GsE were observed by transmission electron microscopy (Tecnai G2 F30, FEI, Eindhoven, Netherlands). The particle size distribution and ζ-potential of CMSN, GsE, and CMSN@GsE were measured by Nano-ZS90 Nanosizer (Malvern Instruments Ltd., Worcestershire, UK). The specific surface area, pore size, and pore volume of these preparations were measured by an adsorption analyzer (V-Sorb 2800 P, Gold APP Instrument Corporation, Beijing, China). Furthermore, the changes in the microscopic morphology of ICG/CMSN before and after encapsulation of exosomes were also observed by atomic force microscopy (Cypher ES, Asylum Research Ltd., USA). A UV–Vis–NIR spectrometer was also used to scan the spectra of ICG, CMSN, GE, ICG/CMSN, and ICG/CMSN@GE in the wavelength range of 300 nm–1000 nm to verify that ICG/CMSN@GE was successfully assembled. Finally, the GE and CMSN@GE extracted proteins were validated by SDS-PAGE (DYY-6C, Liuyi Biotechnology Co., Ltd., Beijing, China) to examine whether the signature proteins

changed before and after GE coating.

4.7. Storage stability of ICG/CMSN@GsE and stability of ICG improved by CMSN@GsE

The storage stability of ICG/CMSN@GsE in PBS and 10% FBS was studied for 7 days when stored at 4 °C and the size and distribution were measured by DLS to monitor the changes. In addition, the free ICG, ICG/CMSN, and ICG/CMSN@GsE were dispersed in aqueous solutions and stored in the dark for 5 days, and their UV–vis–NIR spectra were scanned every day. Meanwhile, the light stability of free ICG, ICG/CMSN, and ICG/CMSN@GsE were performed in aqueous solutions under sunlight for 3 h, and their UV–vis–NIR spectra were recorded every 1 h.

4.8. ROS detection in vitro

The ROS generation ability of ICG/CMSN@GsE was detected by a 1,3-diphenylbenzofuran (DPBF) probe. Especially, 200 μL DPBF methanol solution (150 μg/mL) was mixed with 2.8 mL free ICG, ICG/CMSN, and ICG/CMSN@GsE (5 μg/mL ICG) solutions respectively, and then irradiated with an 808 nm laser (0.75 W/cm^2) for different periods (0, 2, 4, 6, 8, 10 min). The corresponding UV–vis absorption curves of DPBF were obtained using a UV–vis spectrophotometer.

4.9. Cell culture and tumor model

RAW 264.7 cells were cultured in high-glucose DMEM and treated with 40 ng/mL of IL-4 for 48 h to obtain M2-like macrophages and 4T1 cells were cultured in the RPMI-1640 medium. All media contained 10% fetal bovine serum (FBS) and 1% penicillin-streptomycin.

Female BALB/c mice (6–8 weeks) were purchased from Shenyang Laboratory Animal Center. 100 μL 4T1 cells (1×10^6) were injected subcutaneously into the right-hand side thigh of the mouse to construct the 4T1 tumor-bearing mouse model. The tumor volumes were measured using the vernier caliper and calculated with the following equation: $V = A \cdot B^2/2$, where A and B represent the longest and shortest diameter of the tumor, respectively. The mice were used for the subsequent experiments until the volume of the tumor reached around 100 mm^3.

4.10. In vitro cellular uptake

The targeting uptake of CMSN@GsE by M2-like macrophages was evaluated by FCM and CLSM. Briefly, the RAW264.7 cells were polarized into M2 phenotype by IL-4 as described above and then the M2-like macrophages and 4T1 cells were co-cultured in a 6-well plate and treated with CMSN and CMSN@GsE (CMSN was labeled with Cy5 and the concentration was 20 μg/mL) for 3 h. Followed by digestion and centrifugation (1500 rpm, 3 min), the M2-like macrophages were labeled with anti-F4/80 antibody, and the uptake of CMSN and CMSN@GsE by the two different cells was detected by FCM. In addition, M2-like macrophages and 4T1 cells were respectively cultured with CMSN@GsE (CMSN was labeled with Cy5, GsE was labeled with Dil) for 2 h. Further, the two cells were stained with Hoechst 33,342 and WGA (the nucleus was labeled with Hoechst, and the cell membrane was labeled with WGA), and the fluorescence images were observed by CLSM to analyze the difference of internalization of CMSN@GsE in two kinds of cells.

To explore the endocytosis pathway of CMSN@GsE, 4T1 cells, and M2-like macrophages were inoculated in 6-well plates separately and pretreated with transport inhibitors such as amiloride hydrochloride (EIPA), genistein, dynamin (dynasore), nystatin, or chlorpromazine (CPZ) for 1 h. The cells were then incubated with Cy5-labeled CMSN@GsE (100 μg/mL). Finally, cells were washed with cold PBS, digested, and harvested for analysis by flow cytometry.

4.11. In vivo imaging and biodistribution analysis

ICG/CMSN and ICG/CMSN@GsE (ICG: 2.5 mg/kg) nanoparticles were injected into tumor-bearing mice through the tail vein, and fluorescence intensities of ICG were observed by an *in vivo* imaging system (Bruker MI SE, Germany) at 1, 3, 6,12, 24 h post-administration. Subsequently, the mice were sacrificed at 24 h post-injection, and main organs (heart, liver, spleen, lung, and kidney) and tumor tissues were collected for *ex vivo* imaging to analyze drug distribution and penetration effects within the tumor *in vivo*.

4.12. Cell viability measurement

To ensure that ICG/CMSN@GsE could repolarize macrophages as much as possible and limit the toxicity of ROS, a CCK-8 cell viability assay was carried out to determine the optimal drug-loading efficiency and concentration of ICG. The M2-like macrophages were seeded in a 96-well plate (5×10^3 cells/well) for 12 h and further incubated with ICG/CMSN@GsE of various drug-loading efficiency (1%, 3%, 5% and 10%) at different concentrations of ICG (2, 4, 6, 8, 10, 15, 20 μg/mL) for 6 h. Following illuminating with 808 nm laser (0.75 W/cm^2) for 3 min, the M2-like macrophages were incubated continually in fresh medium for another 24 h, then the cell viability was analyzed using CCK-8 assay kits.

4.13. In vitro analysis of M2-like macrophage repolarization

The M2-like macrophages were exposed to (1) Saline, (2) ICG, (3) ICG/CMSN, (4) GsE, (5) ICG/CMSN + GsE, (6) ICG/CMSN@GsE for 6 h followed by irradiating with an 808 nm laser (0.75 W/cm^2, 3 min) for the groups containing ICG. Afterwards, the cells were washed twice with PBS and cultured for another 24 h. Then, stained with mouse anti-CD86-APC, and anti-CD206-PE for 30 min at 4 °C, the cells were analyzed by FCM. The supernatants were collected and stored at - 80 °C for further use.

4.14. Transcriptome analysis of M2-like macrophages treated with ICG/CMSN or ICG/CMSN@GsE

M2-like macrophages were inoculated in 6-well plates at a density of 2×10^5 cells/well, and ICG/CMSN and ICG/CMSN@GE nanohybrids were added to the corresponding wells (the final concentration of ICG was 15 μg/mL for each), and the cells were incubated for 6 h at 37 °C in light-protected culture, and then replaced by fresh culture medium, and irradiated by NIR with a power density of 0.75 W/cm^2 for 3 min, and then continued to be incubated. After 24 h, the cells were collected and added with RNAiso Plus (Takara, Japan) for subsequent treatment.

4.15. The damage of ICG/CMSN@GsE to 4T1 cells in vitro

4T1 cells were seeded in 6 well plates at a density of 1×10^5 cells per well and cultured overnight at 37 °C. Then the supernatants collected above were added to 4T1 cells. The untreated cell was regarded as a negative control. After being incubated for 24 h, the cells were washed once with PBS and stained with 100 mL binding buffer containing 5 μL Annexin V-FITC and 5 μL PI for 15 min followed by adding 400 μL binding buffer to detect cell apoptosis by FCM.

4.16. Enzyme-linked immunosorbent assay (ELISA)

M2-like macrophages were incubated with ICG, CMSN, ICG/CMSN, ICG/CMSN@GsE, and ICG/CMSN@GsE (0.75 W/cm^2, 3 min) respectively for 6 h. Afterwards, the cells were washed with PBS three times and incubated for a further 24 h. Then cell supernatant in each group was collected for measuring the expression level of NO, TNF-α, and IL-12 proinflammatory cytokines via ELISA kits by production guidelines.

4.17. In vivo tumor therapy

BALB/c mice bearing subcutaneous tumors were randomly divided into 6 groups (n = 5), including (1) Saline, (2) ICG, (3) ICG/CMSN, (4) GsE, (5) ICG/CMSN + GsE, (6) ICG/CMSN@GsE. Each mouse was injected with 100 μL of nanodrug suspension via the tail vein every two other days for 4 times in total (ICG:1 mg/kg body weight). And for the laser treatment groups, an 808 nm laser was used to irradiate the tumor site with a power density of 0.75 W/cm^2 for 5 min at 3 h post the administration. The weight and tumor volume of mice were measured every 2 days, which were used to evaluate the anti-tumor effects. Finally, the mice were euthanized on day 18 after the first treatment, and the tumors were obtained and further fixed with 4% paraformaldehyde for immunofluorescence staining of F4/80, CD206 and CD86 to label total macrophages, M2-like and M1-like macrophages, respectively. Meanwhile, the apoptosis of tumor tissues was evaluated by TUNEL. In addition, the main organs (heart, liver, spleen, lung, and kidney) of mice in different groups were harvested for hematoxylin-eosin (H&E) staining according to the standard protocol.

4.18. Statistical methods

Quantitative data were expressed as Mean $\pm$ SD. Two-tailed *t*-test was used for two-group comparison. One-way ANOVA analysis was used for multiple-group comparison. Statistical significance was set at *p < 0.05, **p < 0.01, ***p < 0.001, and ns., not significant.

5. Ethics approval and consent to participate

The study utilized male BALB/c mice (age, 6–8 weeks) obtained from Liaoning Changsheng Biotechnology Co., Ltd. (Liaoning, China). The mice were housed in a controlled environment that was free from pathogens, with regulated lighting and temperature conditions. All animal experiments were performed according to the guidelines approved by the Institutional Animal Use Committee of Shenyang Pharmaceutical University and the National Research Council's Guide for the Care and Use of Laboratory Animals.

CRediT authorship contribution statement

Wei Gu: Writing – review & editing, Visualization, Supervision, Formal analysis, Data curation. **Wen Guo:** Writing – review & editing, Writing – original draft. **Zhishuang Ren:** Visualization, Project administration, Formal analysis, Data curation. **Yimeng Zhang:** Visualization, Project administration, Formal analysis. **Meiqi Han:** Investigation, Data curation. **Qinfu Zhao:** Project administration. **Yikun Gao:** Project administration. **Yuling Mao:** Writing – review & editing, Visualization, Supervision, Project administration, Investigation, Funding acquisition, Formal analysis, Data curation. **Siling Wang:** Visualization, Supervision, Project administration, Methodology, Funding acquisition, Formal analysis, Conceptualization.

Declaration of competing interest

The authors declare that they have no known competing financial interests or personal relationships that could have appeared to influence the work reported in this paper.

Appendix A. Supplementary data

Supplementary data to this article can be found online at https://doi.

org/10.1016/j.bioactmat.2024.04.029.

References

[1] I. Vitale, G. Manic, L.M. Coussens, G. Kroemer, L. Galluzzi, Macrophages and metabolism in the tumor microenvironment, Cell Metabol. 30 (1) (2019) 36–50.

[2] V. Gambardella, J. Castillo, N. Tarazona, F. Gimeno-Valiente, T. Fleitas, The role of Tumor-Associated Macrophages in Gastric Cancer development and their potential as a therapeutic target, Cancer Treat Rev. 86 (2020) 102015.

[3] E. Nasrollahzadeh, S. Razi, M. Keshavarz-Fathi, M. Mazzone, N. Rezaei, Pro-tumorigenic functions of macrophages at the primary, invasive and metastatic tumor site, Cancer Immunol. Immunother. 69 (2) (2020).

[4] H. Luo, H. Zhang, J. Mao, H. Cao, Y. Tao, G. Zhao, Z. Zhang, N. Zhang, Z. Liu, J. Zhang, Exosome-based nanoimmunotherapy targeting TAMs, a promising strategy for glioma, Cell Death Dis. 14 (4) (2023).

[5] N. Kumari, S.H. Choi, Tumor-associated macrophages in cancer: recent advancements in cancer nanoimmunotherapies, J. Exp. Clin. Cancer Res. 41 (1) (2022) 68.

[6] R. Zhang, T. Wang, Q. Lin, 847 Inflammasome activation in M2 macrophage restrain the immune suppressive function, Journal for ImmunoTherapy of Cancer (2020).

[7] X. Sun, J. Gao, X. Meng, X. Lu, L. Zhang, R. Chen, Polarized macrophages in periodontitis: characteristics, function, and molecular signaling, Front. Immunol. 12 (2021).

[8] Ngambenjawong Chayanon, Cieslewicz Maryelise, G. Joan, Suzie Schellinger, H. Pun, Synthesis and evaluation of multivalent M2pep peptides for targeting alternatively activated M2 macrophages, J. Contr. Release (2016).

[9] N. Anand, K.H. Peh, J.M. Kolesar, Macrophage repolarization as a therapeutic strategy for osteosarcoma, Int. J. Mol. Sci. (2023).

[10] J. Liu, Y. Wei, Y. Wu, J. Li, J. Sun, G. Ren, H. Li, ATP2C2 has potential to define tumor microenvironment in breast cancer, Front. Immunol. 12 (2021).

[11] D. Hongliang, Y. Yueyao, G. Chenhui, S. Hehe, W. Hongmin, H. Chao, W. Jun, G. Fangyuan, G. Xiaoming, Lactoferrin-containing immunocomplex mediates antitumor effects by resetting tumor-associated macrophages to M1 phenotype, Journal for ImmunoTherapy of Cancer 8 (1) (2020) e000339.

[12] Y. Zhang, Z. Feng, J. Liu, H. Li, Q. Su, J. Zhang, P. Huang, W. Wang, J. Liu, Polarization of tumor-associated macrophages by TLR7/8 conjugated radiosensitive peptide hydrogel for overcoming tumor radioresistance, Bioact. Mater. 16 (2022) 359–371.

[13] X. Wang, Y. Cheng, X. Han, J. Yan, Y. Wu, P. Song, Y. Wang, X. Li, H. Zhang, Functional 2D iron-based nanosheets for synergistic immunotherapy, phototherapy, and chemotherapy of tumor, Adv. Healthcare Mater. 11 (19) (2022) 2200776.

[14] H. Xiao, Y. Guo, B. Li, X. Li, Y. Wang, S. Han, D. Cheng, X. Shuai, M2-like tumor-associated macrophage-targeted codelivery of STAT6 inhibitor and IKKβ siRNA induces M2-to-M1 repolarization for cancer immunotherapy with low immune side effects, ACS Cent. Sci. 6 (7) (2020) 1208–1222.

[15] Q. Shou, H. Fu, X. Huang, Y. Yang, PARP-1 controls NK cell recruitment to the site of viral infection, Jci Insight 4 (12) (2019).

[16] X. Li, R. Liu, Y. Wang, W. Zhu, D. Zhao, X. Wang, H. Yang, E.C. Gurley, W. Chen, P. B. Hylemon, Cholangiocyte-derived exosomal lncRNA H19 promotes macrophage activation and hepatic inflammation under cholestatic conditions, Cells 9 (1) (2020) 190.

[17] Y. An, H. Zhang, C. Wang, F. Jiao, H. Xu, X. Wang, W. Luan, F. Ma, L. Ni, X. Tang, Activation of ROS/MAPKs/NF-κB/NLRP3 and inhibition of efferocytosis in osteoclast-mediated diabetic osteoporosis, Faseb. J. 33 (11) (2019) 12515.

[18] C. Li, Z. Li, S. Xun, P. Jiang, R. Yan, M. Chen, F. Hu, R.A. Rupp, X. Zhang, L. Pan, Protection of the biconcave profile of human erythrocytes against osmotic damage by ultraviolet-A irradiation through membrane-cytoskeleton enhancement, Cell Death Discovery 3 (1) (2017) 1–10.

[19] W. Li, X. Geng, D. Liu, Z. Li, Near-infrared light-enhanced protease-conjugated gold nanorods as a photothermal antimicrobial agent for elimination of exotoxin and biofilms, Int. J. Nanomed. (2019) 8047–8058.

[20] S. Guo, D. Gu, Y. Yang, J. Tian, X. Chen, Near-infrared photodynamic and photothermal co-therapy based on organic small molecular dyes, J. Nanobiotechnol. 21 (1) (2023) 348.

[21] W. Zhu, Visualizing deeper into the body with a NIR-II small-molecule fluorophore, Sci. China Chem. 59 (2) (2016) 203–204.

[22] Z. Yu, W. Pan, N. Li, B. Tang, A nuclear targeted dual-photosensitizer for drug-resistant cancer therapy with NIR activated multiple ROS, Chem. Sci. 7 (7) (2016) 4237–4244.

[23] S. Gao, Y. Liu, M. Liu, D. Yang, M. Zhang, K. Shi, Biodegradable mesoporous nanocomposites with dual-targeting function for enhanced anti-tumor therapy, J. Contr. Release 341 (2022) 383–398.

[24] R. Alford, H.M. Simpson, J. Duberman, G.C. Hill, M. Ogawa, C. Regino, H. Kobayashi, P.L. Choyke, Toxicity of organic fluorophores used in molecular imaging: literature review, Mol. Imag. 8 (6) (2009) 00031, 7290.2009.

[25] S. Mindt, I. Karampinis, M. John, M. Neumaier, K. Nowak, Stability and degradation of indocyanine green in plasma, aqueous solution and whole blood, Photochem. Photobiol. Sci. 17 (2018) 1189–1196.

[26] H. Wang, X. Li, B.W.-C. Tse, H. Yang, C.A. Thorling, Y. Liu, M. Touraud, J. B. Chouane, X. Liu, M.S. Roberts, Indocyanine green-incorporating nanoparticles for cancer theranostics, Theranostics 8 (5) (2018) 1227.

[27] V. Saxena, M. Sadoqi, J. Shao, Degradation kinetics of indocyanine green in aqueous solution, J. Pharmaceut. Sci. 92 (10) (2003) 2090–2097.

[28] J. Fu, B. Wu, M. Wei, Y. Huang, Y. Zhou, Q. Zhang, L. Du, Prussian blue nanosphere-embedded in situ hydrogel for photothermal therapy by peritumoral administration, Acta Pharm. Sin. B 9 (3) (2019) 604–614.

[29] Y. Qiu, Z. Wu, Y. Chen, J. Liao, Q. Zhang, Q. Wang, Y. Duan, K. Gong, S. Chen, L. Wang, Nano ultrasound contrast agent for synergistic chemo-photothermal therapy and enhanced immunotherapy against liver cancer and metastasis, Adv. Sci. (2023) 2300878.

[30] R. Kalluri, The biology and function of exosomes in cancer, The Journal of clinical investigation 126 (4) (2016) 1208–1215.

[31] F. Xie, X. Zhou, M. Fang, H. Li, P. Su, Y. Tu, L. Zhang, F. Zhou, Extracellular vesicles in cancer immune microenvironment and cancer immunotherapy, Adv. Sci. 6 (24) (2019) 1901779.

[32] M.-Y. Li, L.-Z. Liu, M. Dong, Progress on pivotal role and application of exosome in lung cancer carcinogenesis, diagnosis, therapy and prognosis, Mol. Cancer 20 (2021) 1–22.

[33] X. Zhuang, Y. Teng, A. Samykutty, J. Mu, Z. Deng, L. Zhang, P. Cao, Y. Rong, J. Yan, D. Miller, Grapefruit-derived nanovectors delivering therapeutic miR17 through an intranasal route inhibit brain tumor progression, Mol. Ther. 24 (1) (2016) 96–105.

[34] N. Mu, J. Li, L. Zeng, J. You, R. Li, A. Qin, X. Liu, F. Yan, Z. Zhou, Plant-derived exosome-like nanovesicles: current progress and prospects, Int. J. Nanomed. (2023) 4987–5009.

[35] Y. Cai, L. Zhang, Y. Zhang, R. Lu, Plant-derived exosomes as a drug-delivery approach for the treatment of inflammatory bowel disease and colitis-associated cancer, Pharmaceutics 14 (4) (2022) 822.

[36] M. Cao, H. Yan, X. Han, L. Weng, Q. Wei, X. Sun, W. Lu, Q. Wei, J. Ye, X. Cai, Ginseng-derived nanoparticles alter macrophage polarization to inhibit melanoma growth, Journal for immunotherapy of cancer 7 (1) (2019).

[37] D. Tarn, C.E. Ashley, M. Xue, E.C. Carnes, J.I. Zink, C.J. Brinker, Mesoporous silica nanoparticle nanocarriers: biofunctionality and biocompatibility, Accounts of chemical research 46 (3) (2013) 792–801.

[38] S. Li, R. Chang, L. Zhao, R. Xing, J.C. van Hest, X. Yan, Two-photon nanoprobes based on bioorganic nanoarchitectonics with a photo-oxidation enhanced emission mechanism, Nat. Commun. 14 (1) (2023) 5227.

[39] S. Kamerkar, C. Leng, O. Burenkova, S.C. Jang, C. McCoy, K. Zhang, K. Dooley, S. Kasera, T. Zi, S. Sisó, Exosome-mediated genetic reprogramming of tumor-associated macrophages by exoASO-STAT6 leads to potent monotherapy antitumor activity, Sci. Adv. 8 (7) (2022) eabj7002.

[40] H. Liu, F. Qian, Exploiting macropinocytosis for drug delivery into KRAS mutant cancer, Theranostics 12 (3) (2022) 1321.

[41] X. Wu, Y. Zhu, W. Huang, J. Li, B. Zhang, Z. Li, X. Yang, Hyperbaric oxygen potentiates doxil antitumor efficacy by promoting tumor penetration and sensitizing cancer cells, Adv. Sci. 5 (8) (2018) 1700859.

[42] J. Kim, Y. Zhu, S. Chen, D. Wang, S. Zhang, J. Xia, S. Li, Q. Qiu, H. Lee, J. Wang, Anti-glioma effect of ginseng-derived exosomes-like nanoparticles by active blood–brain-barrier penetration and tumor microenvironment modulation, J. Nanobiotechnol. 21 (1) (2023) 253.

[43] Z. Yan, H. Luo, B. Xie, T. Tian, S. Li, Z. Chen, J. Liu, X. Zhao, L. Zhang, Y. Deng, Targeting adaptor protein SLP76 of RAGE as a therapeutic approach for lethal sepsis, Nat. Commun. 12 (1) (2021) 308.

[44] S.C.-C. Huang, B. Everts, Y. Ivanova, D. O'sullivan, M. Nascimento, A.M. Smith, W. Beatty, L. Love-Gregory, W.Y. Lam, C.M. O'neill, Cell-intrinsic lysosomal lipolysis is essential for alternative activation of macrophages, Nat. Immunol. 15 (9) (2014) 846–855.

[45] Y. Yang, M. Sun, W. Yao, F. Wang, X. Li, W. Wang, J. Li, Z. Gao, L. Qiu, R. You, Compound kushen injection relieves tumor-associated macrophage-mediated immunosuppression through TNFR1 and sensitizes hepatocellular carcinoma to sorafenib, Journal for immunotherapy of cancer 8 (1) (2020).

[46] X. Wang, W. Guo, J. Han, L. Yi, Q. Zhao, Y. Mao, S. Wang, Oral spatial-to-point cascade targeting "sugar-coated bullets" for precise and safe chemotherapy by intervention Warburg effect, Colloids Surf. B Biointerfaces 222 (2023) 113108.